J Mater Sci (2011) 46:3708–3715
DOI 10.1007/s10853-010-5143-7

Deformation behavior of an Al–Cu–Mg–Mn–Zr alloy during hot compression

Yao Li · Zhiyi Liu · Lianghua Lin · Jiangtao Peng · Ailin Ning

Received: 2 September 2010 / Accepted: 30 November 2010 / Published online: 14 December 2010

Abstract Deformation behavior of an Al–Cu–Mg–Mn–Zr alloy during hot compression was characterized in present work by high-temperature testing and transmission electron microscope (TEM) studies. The true stress–true strain curves exhibited a peak stress at a critical stain. The peak stress decreased with increasing deformation temperature and decreasing strain rate, which can be described by Zener–Hollomon (Z) parameter in hyperbolic sine function with the deformation activation energy 277.8 kJ/mol. The processing map revealed the existence of an optimum hot-working regime between 390 and 420 °C, under strain rates ranging from 0.1 to 1 s^{-1}. The main softening mechanism of the alloy was dynamic recovery at high ln$Z$ value; continuous dynamic recrystallization (DRX) occurred as deformed at low ln$Z$ value. The dynamic precipitation of Al_3Zr and $Al_{20}Cu_2Mn_3$ dispersoids during hot deformation restrained DRX and increased the hot deformation activation energy of the alloy.

Y. Li · Z. Liu (✉) · L. Lin · J. Peng
Key Laboratory of Nonferrous Metal Materials Science and Engineering, Ministry of Education, Central South University, Changsha 410083, China
e-mail: liuzhiyi@mail.csu.edu.cn

Y. Li · Z. Liu · L. Lin · J. Peng
School of Materials Science and Engineering, Central South University, Changsha 410083, China

A. Ning
Department of Mechanical and Energy Engineering, Shaoyang University, Shaoyang 422004, China

Introduction

Alloys based on the Al–Cu–Mg system are widely used in the commercial aircraft structures such as fuselage and lower wing surface because of their high strength to weight ratio, superior high-temperature properties, good damage tolerance, resistance to fatigue crack propagation, and fracture toughness [1–4]. The 2xxx aluminum alloys are frequently formed by hot rolling, extrusion or forging; the intermediate and high forming temperatures result in a number of different microstructural processes that significantly influence the final mechanical response of the alloy [5]. In order to obtain a good combination of mechanical properties and microstructure, it is important to understand hot workability and microstructural evolution of Al–Cu–Mg alloys during hot deformation.

Previous investigations suggested that thermomechanical parameters and micro-alloying had significant effects on flow behavior and microstructural evolution during high-temperature deformation [6–8]. Liu et al. [6] reported that the softening mechanism of Al–Cu–Mg–Ag alloy transformed from dynamic recovery (DRV) to dynamic recrystallization (DRX) with decreasing Z (Zener–Hollomon parameter) value and the volume fraction of DRX grains increased with increasing the deformation temperature and decreasing the strain rate. However, Li et al. [7] investigated the hot deformation behavior and microstructural evolution of 2519 Al alloy at temperatures of 300–500 °C and nominal strain rates of 0.01–10 s^{-1}, and found that DRX occurred in the alloy at high temperature and high strain rate. Trace additions of Sn (0.06 wt%) to Al–Cu–Mg alloy resulted in an increase of peak stress and deformation activation energy as suggested by Banerjee et al. [8]. Besides, many investigations also found that dynamic precipitation (DPN) occurred during hot deformation in 2024 [9], 2026 [10],

2618 [5], Al–Mg–Si–Cu [11], and Al–Mg–Er [12] alloys. The precipitation of second phase particles affected the flow curve shape and stress level. Jin et al. [13] reported the DPN and subsequent coarsening of precipitates during hot compression deformation have been assumed to be responsible for the flow softening of the 7150 Al alloy at high Z value.

Small additions of Mn and Zr are well known to reduce the grain size and to increase the resistance to recrystallization of high-strength aluminum alloys, by forming a stable dispersion of $Al_{20}Cu_2Mn_3$ and Al_3Zr particles [14, 15]. The effectiveness of the dispersoid depends on their size, spacing, and distribution. In commercial practice, the $Al_{20}Cu_2Mn_3$ and Al_3Zr dispersoids are generally precipitated during homogenization. Dispersoids cannot be dissolved to an appreciable extent by subsequent solid state thermal treatments due to the low solubility of the main dispersoid forming elements Mn and Zr [16]. Small Al_3Zr dispersoid particles inhibited recrystallization by pinning grain and subgrain boundaries during hot deformation [17]. Although DPN of $Al_{20}Cu_2Mn_3$ particles had been reported in Ref. [10], studies of DPN of Al_3Zr particles during hot deformation are limited.

The processing map is very beneficial for optimizing hot workability and controlling microstructure. The validity of processing maps had been approved in many alloys such as Co–Cr–Mo, Al–Li, Ni–Cr–Mo–W, Mg–Zn–Ce, and Fe–Al–Cr alloys [18–22], but investigations on the processing map of Al–Cu–Mg–Mn–Zr alloy are still rare. Therefore, the aim of the present study was to investigate the deformation characteristic, processing map, and microstructural evolution of Al–Cu–Mg–Mn–Zr alloy during hot compression. In addition, the constitutive equations were determined for the alloy by using the experimental data. Effects of DPN of $Al_{20}Cu_2Mn_3$ and Al_3Zr particles on the flow curves and hot deformation activation energy were also discussed in detail.

Experimental procedures

The chemical composition of experimental alloy used in this study was Al–3.78Cu–1.67Mg–0.67Mn–0.13Zr (wt%). The ingot was homogenized at 490 °C for 24 h. Cylindrical specimens 15 mm in height and 10 mm in diameter were machined from the homogenized material and both ends of each specimen were recessed to a depth of 0.2 mm to entrap the lubricant for compression. A graphite lubricant was used to reduce the friction during compression.

Hot compression tests were performed on a Gleeble 1500 mechanical testing machine in the temperature range of 350–450 °C and under a true strain rate ranging from 0.001 to 1 s^{-1}. Samples were heated to test temperature at a heating rate of 200 °C/min and held for 5 min by the thermocouple feedback controlled current before compression. All specimens were deformed to a true strain of 0.5 and immediately water quenched from the test temperature. The deformed specimens were sectioned parallel to the compression axis and the microstructural evolution was monitored by using a FEI TECNAL G^2 transmission electron microscopy (TEM) operating at 200 kV. Specimens for TEM observations were punched mechanically from thin slices with 3 mm in diameter and twin-jet electrolytically polished with a voltage of 10–15 V in a solution of 70% methanol and 30% nitric acid at approximately −20 °C.

Results and discussion

True stress–true strain curves

A series of typical true stress–true strain curves of Al–Cu–Mg–Mn–Zr alloy under different deformation conditions are shown in Fig. 1. It can be seen that the flow stress increased rapidly to a peak at critical stain. The peak stress was the highest for the alloy deformed at 350 °C and strain rate of 1.0 s^{-1}, and decreased with increasing deformation temperature and decreasing strain rate. The critical strain corresponding to the peak stress increased with the decrease of temperature and the increase of strain rate. The rapid rise in flow stress was due to the work hardening at the onset of the deformation. Evident softening occurred as deformed at a relatively low deformation temperature. In contrast, no dramatic softening with increasing strain appeared when deformed at a relatively high deformation temperature. It is hard to identify the actual mechanism of hot working directly from flow curves, so the precise hot deformation mechanism of Al–Cu–Mg–Mn–Zr alloy will be analyzed and discussed by processing map and microstructure observations.

Constitutive equations

In hot deformation of metallic materials, it is commonly accepted that the relationship between the peak stress, strain rate, and deformation temperature can be expressed as [6, 23–25]:

$$\dot{\varepsilon} = A'\sigma^{n_1}\exp\left(-\frac{Q}{RT}\right) \quad (1)$$

$$\dot{\varepsilon} = A''\exp(\beta\sigma)\exp\left(-\frac{Q}{RT}\right) \quad (2)$$

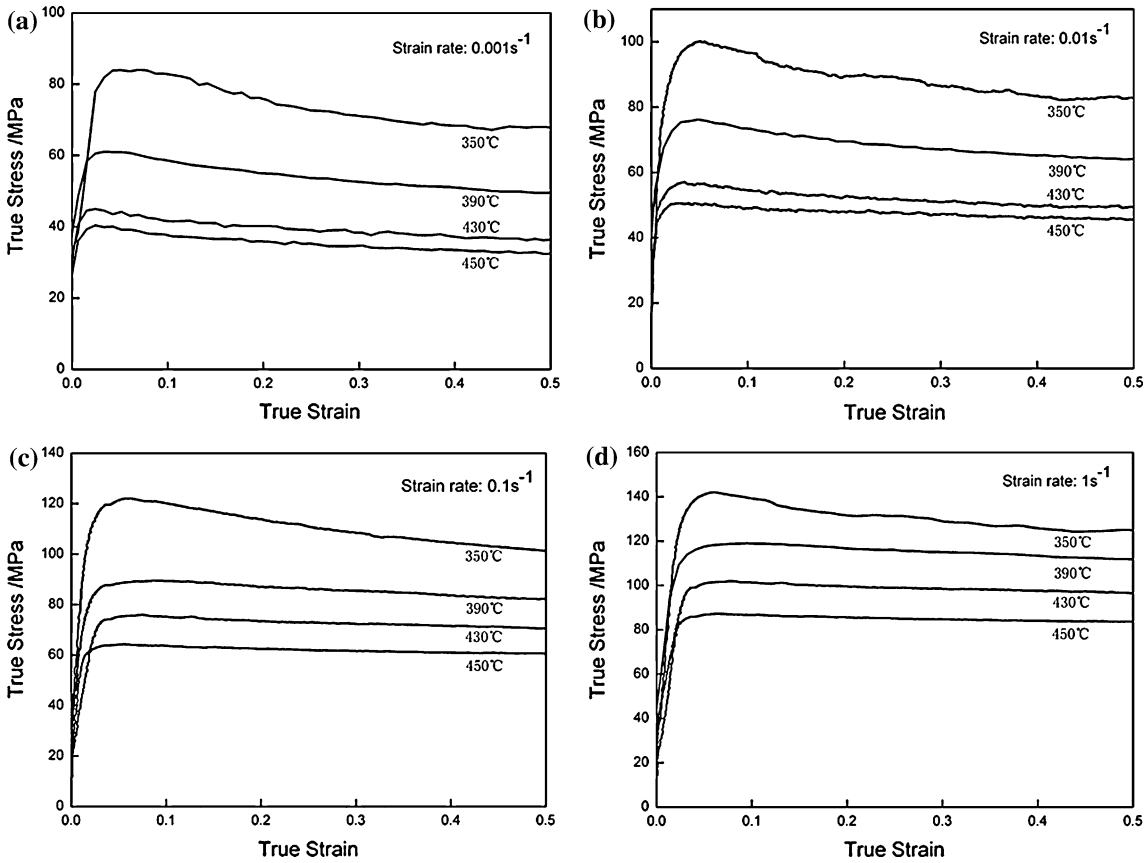

Fig. 1 True stress–true strain curves of Al–Cu–Mg–Mn–Zr alloy during hot compression deformation **a** 0.001 s^{-1}, **b** 0.01 s^{-1}, **c** 0.1 s^{-1}, and **d** 1.0 s^{-1}

$$\dot{\varepsilon} = A[\sinh(\alpha\sigma)]^n \exp\left(-\frac{Q}{RT}\right) \tag{3}$$

$$\alpha = \frac{\beta}{n} \approx \frac{\beta}{n_1} \tag{4}$$

where A', A'', A, n_1, n, β, and α are material constants, Q is the activation energy for hot deformation, R is the gas constant, and T is the deformation temperature. The power law Eq. 1 and the exponential Eq. 2 break at a high stress and at a low stress, respectively. The hyperbolic sine law Eq. 3 is a more general form suitable for stresses over a wide range. By taking natural logarithms for Eqs. 1–3, these expressions can be written as:

$$\ln\dot{\varepsilon} = \ln A_1 - \frac{Q}{RT} + n_1 \ln\sigma \tag{5}$$

$$\ln\dot{\varepsilon} = \ln A_2 - \frac{Q}{RT} + \beta\sigma \tag{6}$$

$$\ln\dot{\varepsilon} = \ln A - \frac{Q}{RT} + n\ln[\sinh(\alpha\sigma)] \tag{7}$$

Q can be expressed as [7, 24]:

$$Q = R\left|\frac{\partial \ln\dot{\varepsilon}}{\partial \ln[\sin(\alpha\sigma)]}\right|_T \left|\frac{\partial \ln[\sin(\alpha\sigma)]}{\partial(1/T)}\right|_{\dot{\varepsilon}} \tag{8}$$

Figure 2 shows the relationship curves among $\dot{\varepsilon}$, σ, and T. It exists an approximate linear relation between strain rate, deformation temperature, and peak stress, which was consistent well with Eqs. 5–7. The material constants and Q value of Al–Cu–Mg–Mn–Zr alloy shown in Table 1 can be obtained by linear regression in Fig. 2 and Eqs. 1–8. The hot deformation activation energy Q is an important parameter serving as an indicator of plasticity [13]. The Q value of Al–3.78Cu–1.67Mg–0.67Mn–0.13Zr alloy is 277.8 kJ/mol, which is higher than that of Al–6.2Cu–0.6Mg alloy (183.38 kJ/mol) and Al–6.2Cu–0.6Mg–0.06Sn alloy (222.3 kJ/mol) [8]. By substituting the above values in Table 1 into Eq. 3, the expression for strain rate is obtained as:

$$\dot{\varepsilon} = 1.47 \times 10^{19}[\sinh(0.0133\sigma)]^{7.9}\exp\left(-\frac{277,800}{RT}\right) \tag{9}$$

The combined effect of strain rate and temperature on deformation behavior can be characterized by Zener–Hollomon (Z) parameter, which is defined as [26, 27]:

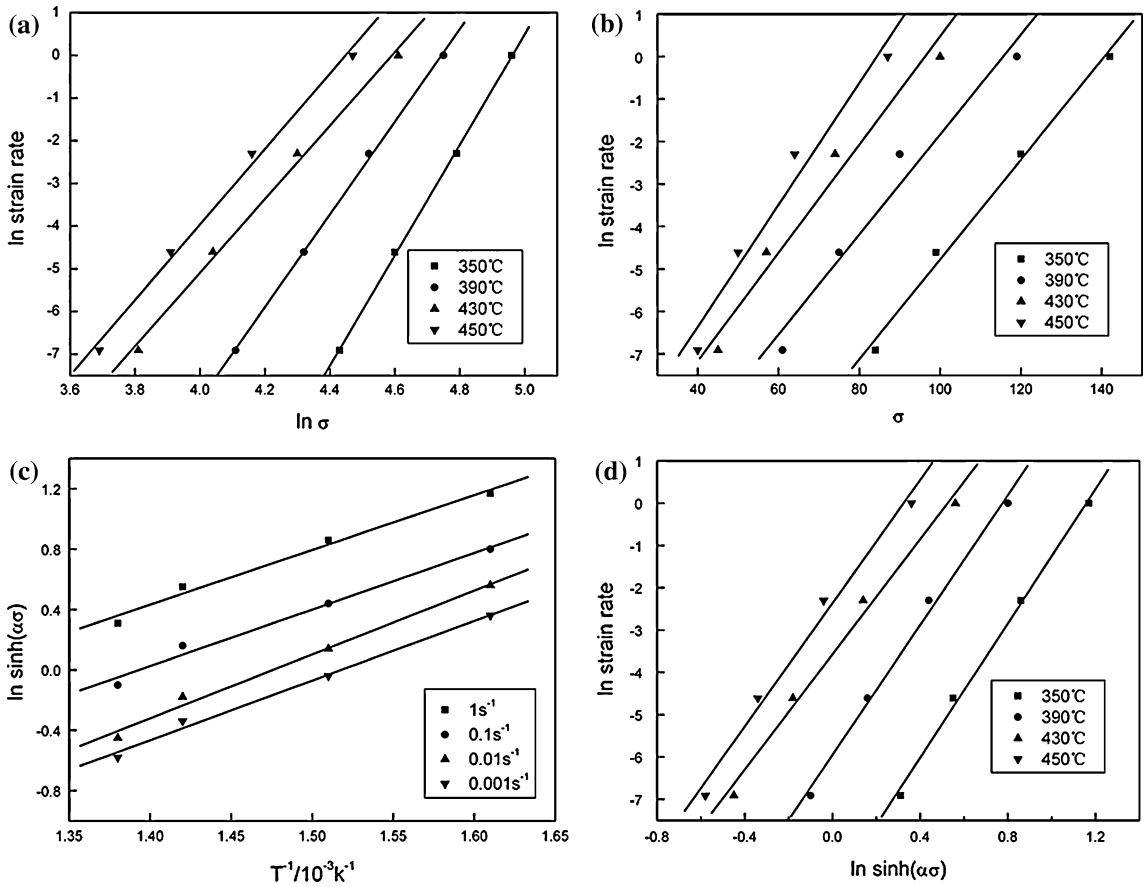

Fig. 2 Relationships among $\dot{\varepsilon}$, σ, T, and Z: **a** $\ln\dot{\varepsilon}$ vs. $\ln\sigma$; **b** $\ln\dot{\varepsilon}$ vs. σ; **c** $\ln\sinh(\alpha\sigma)$ vs. T^{-1}; **d** $\ln\dot{\varepsilon}$ vs. $\ln\sinh(\alpha\sigma)$

Table 1 Material constants and Q value of Al–Cu–Mg–Mn–Zr alloy

A (s^{-1})	α (MPa^{-1})	n	Q (KJ mol^{-1})
1.47×10^{19}	0.0133	7.9	277.8

Table 2 $\ln Z$ values under different deformation conditions, s^{-1}

	0.001 s^{-1}	0.01 s^{-1}	0.1 s^{-1}	1 s^{-1}
350 °C	46.73	49.03	51.33	53.63
390 °C	43.49	45.79	48.09	50.40
430 °C	40.62	42.92	45.23	47.53
450 °C	39.31	41.61	43.91	46.22

$$Z = \dot{\varepsilon}\exp\left(\frac{Q}{RT}\right) = A[\sinh(\alpha\sigma)]^n \tag{10}$$

Table 2 shows the $\ln Z$ values under different hot compression conditions, it is evident that Z increases with decreasing the deformation temperature and increasing the strain rate. Taking the natural logarithm of Eq. 10:

$$\ln Z = \ln A + n\ln[\sinh(\alpha\sigma)] \tag{11}$$

Relationship between $\ln\sinh(\alpha\sigma)$ and $\ln Z$ is shown in Fig. 3, it is found that in the region of temperature and strain rate considered, Z parameter can be used to describe the deformation behavior of Al–Cu–Mg–Mn–Zr alloy effectively.

Processing map

The processing map has been developed on the basis of the dynamic materials model (DMM), which considers the work piece undergoing hot deformation to be a dissipater of power [28]. The power might be instantaneously dissipated into two complementary parts—G content and J content. At any given temperature and strain, the power dissipation between G and J is given by [29]:

$$m = \left.\frac{\partial J}{\partial G}\right|_{\varepsilon,T} = \left.\frac{\partial \ln\sigma}{\partial \ln\dot{\varepsilon}}\right|_{\varepsilon,T}, \tag{12}$$

where m is the strain rate sensitivity of the flow stress. A polynomial equation is used to fit the experimental data (peak stress and strain rate), $\ln\sigma$ can be expressed as:

$$\ln\sigma = a + b\ln\dot{\varepsilon} + c(\ln\dot{\varepsilon})^2 + d(\ln\dot{\varepsilon})^3 \tag{13}$$

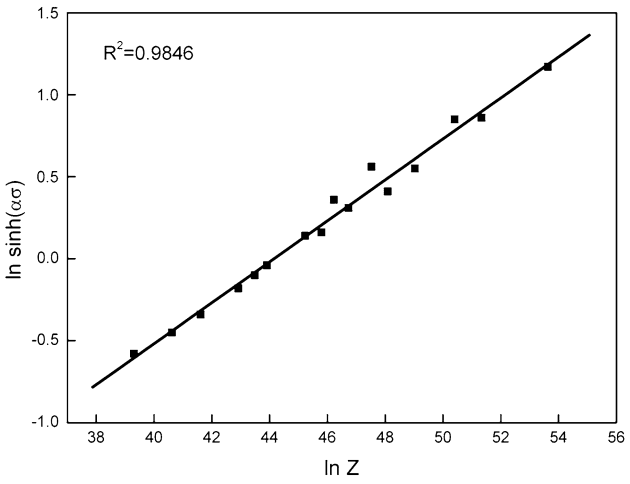

Fig. 3 Relationship between lnsinh($\alpha\sigma$) and ln$Z$

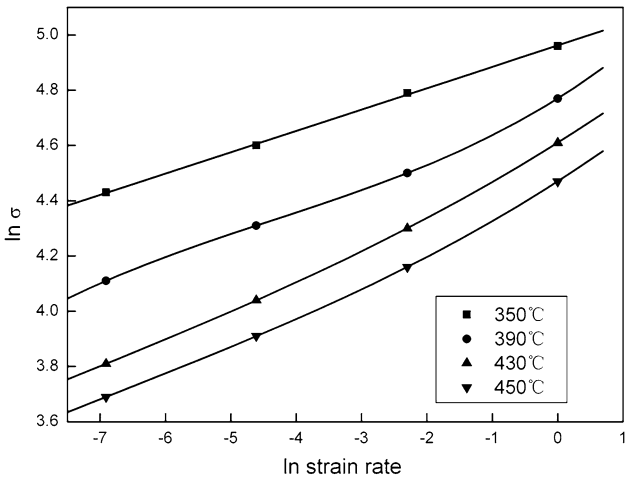

Fig. 4 Relationship between lnσ and ln$\dot{\varepsilon}$

The constants (a, b, c, and d) in Eq. 13 at various deformation temperatures can be obtained by polynomial regression in Fig. 4. Therefore, the strain rate sensitivity m can be calculated by the following equation:

$$m = b + 2c\ln\dot{\varepsilon} + 3d(\ln\dot{\varepsilon})^2 \tag{14}$$

The efficiency of dissipation η is defined as:

$$\eta = \frac{2m}{m+1} \tag{15}$$

Furthermore, the criterion for the onset of flow instability can be written as:

$$\xi(\dot{\varepsilon}) = \frac{\partial \ln(m/(m+1))}{\partial \ln\dot{\varepsilon}} + m \leq 0, \tag{16}$$

where ξ is the instability parameter. The onset of flow instability was observed when $\xi \leq 0$. Similarly, the value of ξ at different deformation conditions can also be calculated by polynomial regression and Eq. 16. The variation

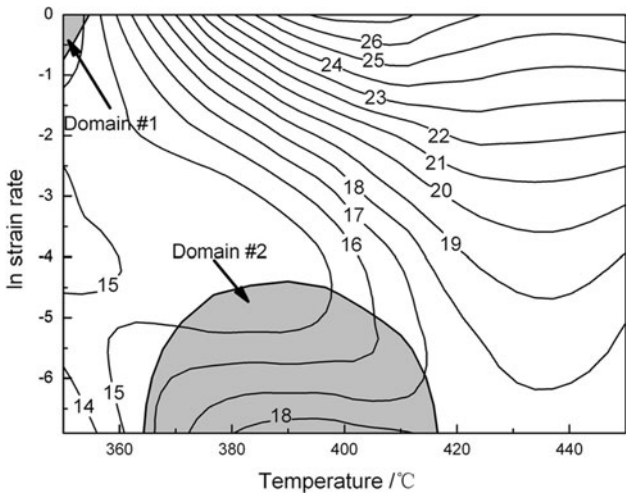

Fig. 5 Processing map for Al–Cu–Mg–Mn–Zr alloy at a strain of 0.5

of η and ξ with temperature and strain rate constitute the power dissipation map and instability map, respectively. The power dissipation map may be superimposed on the instability map to obtain a processing map, which reveals not only the deterministic domains where individual microstructural processes occur, but also the limiting conditions for the regimes of flow instability [28]. Typical processing map generated using the preceding test data at a strain of 0.5 is represented in Fig. 5. The contour numbers represent percent power dissipation efficiency and the shaded domains indicate the regions of flow instability. The processing map exhibits two domains with flow instability. Domain #1 occurs in the temperature range of 350–355 °C and strain rate range of 0.5–1 s^{-1}; domain #2 occurs in the temperature range of 365–418 °C and strain rate range of 0.001–0.01 s^{-1}. These regions of parameters corresponding to flow instability is undesirable for processing and hence should be avoided. The map also exhibits domains at a temperature range of 390–420 °C and a strain rate range of 0.1–1 s^{-1} with a peak efficiency of 27%, which is suitable for hot rolling, extrusion, and forging.

Microstructural evolution

Figure 6 shows a series of TEM micrographs of Al–Cu–Mg–Mn–Zr alloy deformed under different conditions. At high Z value, typically at temperature 350 °C and strain rate of 0.1 s^{-1}, dislocation cells and high dislocation density were detected in Fig. 6a. When ln$Z$ value reached 48.09 (Fig. 6b) or 47.53 (Fig. 6c), dislocations became more active and reorganized through climbing and gliding, resulting in the decrease of dislocation density and the formation of dislocation walls. The dislocation walls segmented the grains, forming a substructure. Thereby the main softening mechanism during hot compression at high

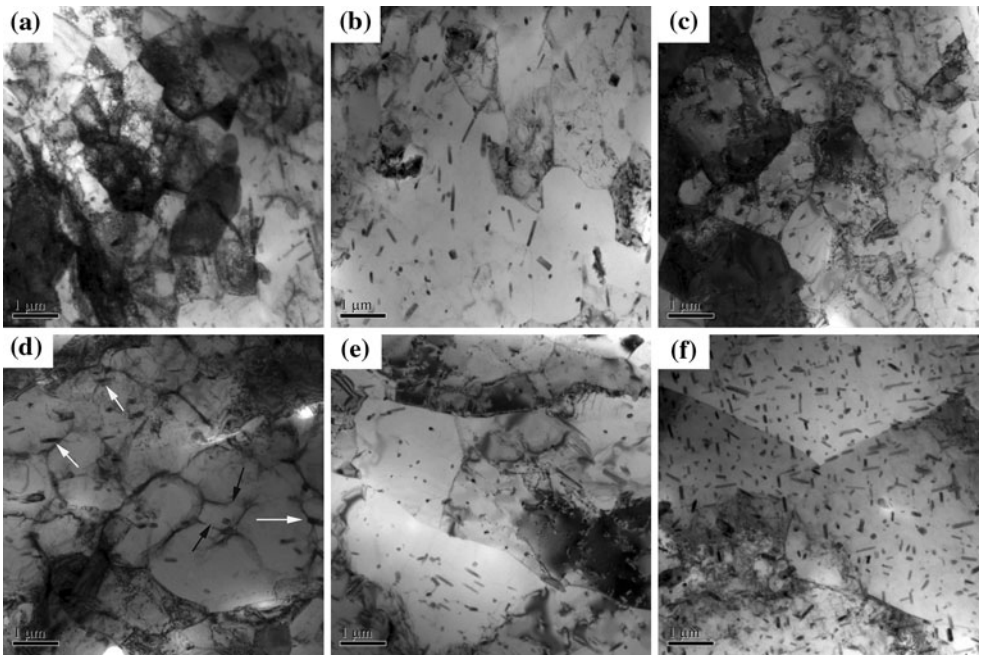

Fig. 6 TEM bright field micrographs of Al–Cu–Mg–Mn–Zr alloy deformed under different conditions: **a** 350 °C, 0.1 s^{-1} ($\ln Z = 51.33$); **b** 390 °C, 0.1 s^{-1} ($\ln Z = 48.09$); **c** 430 °C, 1 s^{-1} ($\ln Z = 47.53$); **d** 430 °C, 0.1 s^{-1} ($\ln Z = 45.23$); **e** 450 °C, 0.1 s^{-1} ($\ln Z = 43.91$); and **f** 430 °C, 0.001 s^{-1} ($\ln Z = 40.62$)

ln*Z* values was DRV, which caused evident softening in the stress–strain curves as compressed at relatively low deformation temperature shown in Fig. 1. With decreasing *Z* value, active dislocations climbing and gliding led to interrupted subgrain boundaries and resultant merging of subgrains, as arrowed in Fig. 6d. Subsequently, a straight and clear grain boundary, accompanied by evident grain growth, formed in Fig. 6e, f. No bulge of grain boundaries was found to occur during hot compression, suggesting continuous dynamic recrystallization (CDRX) occurred.

Moreover, numerous rodlike particles, recognized as $Al_{20}Cu_2Mn_3$ compound [16], were also precipitated during hot compression in this study, especially in the low *Z* regime (Fig. 6f). The high density $Al_{20}Cu_2Mn_3$ particles provided a strong pinning effect for preventing boundary migration as pointed by white arrow in Fig. 6d, which strongly contributed to the CDRX. In addition, DPN was also found to occur for Al_3Zr particles as hot deformed at 450 °C. Figure 7a is TEM images of the sample homogenized at 490 °C for 24 h prior to hot deformation, in which only few Al_3Zr particles were found; in this case the spots associated with Al_3Zr particles were hardly identified in the SAED pattern. Additional precipitation of Al_3Zr particles was observed after deformation at 450 °C under a strain rate of 0.1 s^{-1}, as shown in Fig. 7b. Both microstructural analysis and reflections at the 1/2 $\{002\}_\alpha$ and 1/2 $\{022\}_\alpha$ positions in $\langle 001\rangle_\alpha$ SAED pattern indeed indicated that hot deformation enhanced the precipitation of Al_3Zr particles. Based on the research by Cabibbo et al. [17], the fine Al_3Zr particles that precipitated prior to hot deformation dissolved as the grain boundaries migrated under the imposed external deformation, and re-precipitated behind. In addition, Zr atoms dissolved in the matrix during the initial homogenization stage, can also be used to form Al_3Zr during hot compression. Thus, the increase in the volume fraction of Al_3Zr particles was attributed to the DPN of Al_3Zr during hot compression. Meng et al. [12] also revealed that more dispersed particles with Er were precipitated during hot deformation, which pinned dislocation motion and grain boundary migration, restraining DRX behavior. It can also been confirmed that the dispersed Al_3Zr particles could be dynamically precipitated during hot deformation as a result of the similar precipitation behavior.

Evidently both small dispersed Al_3Zr and $Al_{20}Cu_2Mn_3$ particles, dynamically precipitated at relatively high deformation temperature or low ln*Z* values during hot compression, strongly pinned dislocation cross-slip and grain boundary migration [13, 14, 30], which restrained the DRX. The strong pinning effect on the dislocation cross-slip not only led to the occurrence of no dramatic softening in the flow stress–strain curves illustrated in Fig. 1 under the corresponding deformation conditions, but also increased the deformation activation energy of the alloy, which is much higher than the value for bulk self-diffusion of pure aluminum (143.4 kJ/mol [31]). This reflected the dislocation cross-slip was strongly pinned by dynamically precipitated Al_3Zr and $Al_{20}Cu_2Mn_3$ dispersoids.

Consequently, the evident softening behavior in the stress–strain curves as hot compressed at high ln*Z* value

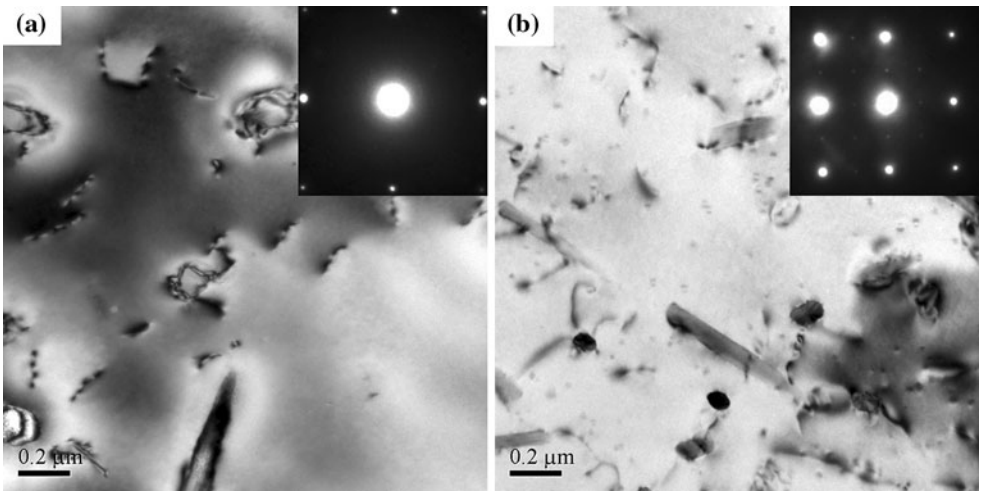

Fig. 7 TEM bright field micrographs and corresponding SAED patterns of specimens **a** homogenized at 490 °C for 24 h, **b** deformed at 450 °C and 0.1 s^{-1}. The electron beam is parallel to $\langle 001 \rangle_{\alpha}$

condition was attributed to DRV, whereas both the absence of any dramatic softening behavior for low Z values and the high deformation activation energy were due to the dynamically precipitated Al_3Zr and $Al_{20}Cu_2Mn_3$ dispersoids pinning dislocations. Moreover, the DPN of Al_3Zr and $Al_{20}Cu_2Mn_3$ particles also pinned grain boundary and retarded boundary migration, resulting in the occurrence of CDRX with merging of subgrains during hot compression.

Conclusion

(1) The flow stress increased rapidly to a peak value at critical stain. The peak stress decreased with increasing deformation temperature and decreasing strain rate, a behavior which can be described by the Zener–Hollomon parameter in hyperbolic sine function with the deformation activation energy 277.8 kJ/mol.

(2) The processing map at a strain of 0.5 suggested that the optimum hot-working conditions for hot rolling, extrusion, and forging were in the temperature range of 390–420 °C and strain rate range of 0.1–1 s^{-1}.

(3) The main softening mechanism of the Al–Cu–Mg–Mn–Zr alloy at high ln$Z$ value was DRV; continuous DRX occurred as deformed at low ln$Z$ value.

(4) Small Al_3Zr and $Al_{20}Cu_2Mn_3$ particles dynamically precipitated during hot deformation restrained DRX and increased the deformation activation energy of the alloy.

Acknowledgements The authors would like to acknowledge the financial support of National Key Fundamental Research Project of China (Grant No. 2005CB623705-04) and Natural Science Foundation of Hunan Province (Grant No. 08JJ3101).

References

1. Williams JC, Starke EA Jr (2003) Acta Mater 51:5775
2. Okayasu M, Sato K, Mizuno M (2008) J Mater Sci 43:2792. doi:10.1007/s10853-008-2544-y
3. Parel TS, Wang SC, Statrink MJ (2010) Mater Des 31:S2
4. Gao N, Starink MJ, Kamp N, Sinclair I (2007) J Mater Sci 42:4398. doi:10.1007/s10853-006-0659-6
5. Cavaliere P (2002) J Light Met 2:247
6. Liu XY, Pan QL, He YB, Li WB, Liang WJ, Yin ZM (2009) Mater Sci Eng A 500:150
7. Li HZ, Li Z, Song M, Liang XP, Guo FF (2010) Mater Des 30:2171
8. Banerjee S, Robi PS, Srinivasan A, Kumar LP (2010) Mater Sci Eng A 527:2498
9. Ebrahimi GR, Zarei-Hanzaki A, Haghshenas M, Arabshahi H (2008) J Mater Proc Technol 206:25
10. Huang XD, Zhang H, Han Y, Wu WX, Chen JH (2010) Mater Sci Eng A 527:485
11. Zhang H, Li LX, Yuan D, Peng DS (2007) Mater Charact 58:168
12. Meng G, Li BL, Li HM, Huang H, Nie ZR (2009) Mater Sci Eng A 516:131
13. Jin NP, Zhang H, Han Y, Wu WX, Chen JH (2009) Mater Charact 60:530
14. Castillo LD, Lavernia EJ (2000) Metall Mater Trans A 31:2287
15. Robson JD, Prangnell PB (2001) Acta Mater 49:599
16. Wang SC, Starink MJ (2005) Int Mater Rev 50:193
17. Cabibbo M, Evangelista E, Spigarell S (2004) Metall Mater Trans A 35:293
18. Chiba A, Lee SH, Matsumoto H, Nakamura M (2009) Mater Sci Eng A 513–514:286
19. Jagan RG, Srinivasana N, Gokhalea AA, Kashyapb BP (2009) J Mater Proc Technol 209:5964
20. Cai DY, Xiong LY, Liu WC, Sun GD, Yao M (2009) Mater Des 30:921
21. Anbuselvan S, Ramanathan S (2010) Mater Des 31:2319
22. Łyszkowski R, Bystrzycki J (2006) Intermetallics 14:1231
23. McQueen HJ, Ryan ND (2002) Mater Sci Eng A 322:43
24. Zong YY, Shan DB, Xu M, Lu Y (2009) J Mater Proc Technol 209:1988
25. El-Danaf EA, AlMajid AA, Soliman MS (2008) J Mater Sci 43:6324. doi:10.1007/s10853-008-2895-4
26. McQueen HJ, Imbert CAC (2004) J Alloys Compd 378:35

27. Spigarelli S, Cabibbo M, Evangelista E (2003) J Mater Sci 38:81. doi:10.1023/A:1021161715742
28. Prasad YVRK, Rao KP (2005) Mater Sci Eng A 391:141
29. Cui C, Schulz A, Epp J, Zoch HW (2010) J Mater Sci 45:2798. doi:10.1007/s10853-010-4269-y
30. Prasad SK, Gokhale AA, Mukhopadhyay AK, Banejee D, Goel DB (1999) Acta Mater 47:2581
31. Mohamed FA, Langdon TG (1974) Met Trans 5:2339